JMEPEG (2009) 18:696–705
DOI: 10.1007/s11665-009-9356-3

1059-9495/$19.00

A Novel SMA-based Concept for Airfoil Structural Morphing

S. Barbarino, R. Pecora, L. Lecce, A. Concilio, S. Ameduri, and E. Calvi

(Submitted September 16, 2008; in revised form November 28, 2008)

The adaptive structures concept is of great interest in the aerospace field because of the several benefits which can be accomplished in the fields including noise reduction, load alleviation, weight reduction, etc., at a level in which they can be considered as compulsory in the design of future aircraft. Improvements in terms of the aerodynamic efficiency, aeroelastic behavior, stability, and manoeuvrability performance have already been proved through many international studies in the past. In the family of the Smart Materials, Shape Memory Alloys (SMA) seem to be a suitable solution for many static applications. Their high structural integrability in conjunction with actuation capabilities and a favorable performance per weight ratio, allows the development of original architectures. In this study, a morphing wing trailing edge concept is presented; morphing ability was introduced with the aim of replacing a conventional flap device. A compliant rib structure was designed, based on SMA actuators exhibiting structural potential (bearing external aerodynamic loads). Numerical results, achieved through a FE approach, are presented in terms of trailing edge induced displacement and morphed shape.

Keywords Aerodynamic surfaces, Morphing, Shape control, SMA

1. Introduction

Because several flight regimes occur during a typical aircraft mission, it is practically impossible to define a single configuration able to maximize aerodynamic efficiency, manoeuvrability, stability, fuel consumption and so on in any circumstance.

Currently, a common design strategy is to identify few dominant flight regimes within a typical mission and define a specific set of parameters like wing body geometry and control surfaces attitude, with respect to which the aircraft performance is maximized. In this way, drawbacks within conditions that fall outside the design range are unavoidable. Solutions characterized by a certain adaptivity level can lead to overcome these limits. Components like ailerons, flaps, equilibrators, together with the related actuation strategies, correspond somehow to the necessity of facing very different states, even dramatically far from the nominal design ones (e.g., take-off and landing) (Ref 1).

To simplify the actuation chain and deform a limited part of the structure, these movable devices are confined to limited regions of the wing; this causes, however, sharp shape modifications, badly affecting the aerodynamic field and, due to the concentration of the external loads around the hinges zone, a significant increase of the structural weight. Classical actuator systems generally lead to a 50% increase in weight relative to a naked wing.

To avoid such problems, different design strategies have been taken into account. An interesting one was implemented within the 3AS (Active Aeroelastic Aircraft Structures) European Project, (Ref 2, 3). By controlling the rigidity of some parts of a wing, the suitable displacement field corresponding to the said optimal configuration for a specific flight regime was attained. This strategy, recalling the classical aeroelastic tailoring philosophy, was applied to an all-movable vertical tail (AMVT), and led to an integrated shaft with a variable stiffness. Instead of using the external loads to deform the aerodynamic surfaces, the so-called 'morphing' strategy may be pursued. In this case, large and distributed deformation of specific parts of the wing body are achieved by generating proper internal forces (Ref 4-6). In order to reach this objective, leading and trailing edges have to be designed to withstand the external loads and undertake dramatic deformations, following the selected flight regime requirements (Ref 7, 8). Large displacement capabilities associated with load bearing capacities is the paradox which the smart or adaptive structure systems have to overcome in order to provide a reliable alternative to classical devices. In this article, the proposed solution to eliminate the above paradox is to refer to actuators that play a structural role, also.

The use of smart materials has a crucial role in this challenging approach. What the authors use in the research

This article is an invited article selected from presentations at Shape Memory and Superelastic Technologies 2008, held September 21-25, 2008, in Stressa, Italy, and has been further expanded from the original presentation.

S. Barbarino, R. Pecora, and **L. Lecce**, Department of Aerospace Engineering, University of Naples "Federico II", Via Claudio 21, Naples 80125, Italy; **A. Concilio** and **S. Ameduri**, Smart Structures Lab., The Italian Aerospace Research Centre (CIRA), Via Maiorise, Capua, 81043 CE, Italy; and **E. Calvi**, ALENIA AERONAUTICA S.p.a., Viale dell'Aeronautica snc, Pomigliano d'Arco, 80038 NA, Italy. Contact e-mail: silvestro.barbarino@gmail.com.

herein presented, are the Shape Memory Alloys, SMA. Their Super Elastic and Shape Memory properties, jointly with their capacity to transmit large loads, make them a privileged material for applications that require both large strains and high actuation forces (hundreds to thousands of Newton for classical commercial elements) (Ref 9).

In this article, the design of an adaptive flap, driven by SMA-based actuators, is illustrated (Ref 10, 11). More in detail, by taking advantage of a FE approach and implementing an SMA descriptive model (Ref 12), the concept of an original rib is dealt with. This structural element is made of different plates that are connected to each other through crossed spring laminas. These are in charge of providing a certain amount of rigidity to the structure, assuring the required preload for the SMA elements and allowing for large relative rotations. SMA elements are wires, located under the springs, which connect two consecutive plates. When they are activated, their contraction leads to a rotation of the rib parts, with consequent camber variations. External aerodynamic loads are considered when the system performance is evaluated; in detail the configuration corresponding to a traditional rotated flap is referred to.

On this architecture, an optimization study is carried out, over certain selected architecture parameters such as the springs, length, their angular position, and location. SMA mechanical properties and geometry are also considered. Results are presented in terms of achievable camber variations and trailing edge displacements.

2. Architecture Working Principle and Modeling Strategy

The considered structure is sketched in Fig. 1. It is made of five bulkily shaped panels, connected in couples by crossed laminas, working as spring elements. The single panel may be assumed to be rigid in the performed study; the set of five constitutes the skeleton of the rib.

The connecting thin plates (beams in a 2D representation, shown in the same figure) exhibit the necessary elastic properties to allow the architecture undergo suitable deflections. Their rigidity is tuned so that deflections related to the external loads are restricted into small fractions of the ones associated with the driving commands.

The proposed actuator system is composed of the union of the active SMA wires and the spring elements. They are thought to show cyclic behavior and to carry out the prescribed external load, i.e., to have a structural purpose that is a function of their characteristic elasticity. These components can be referred to as "bearing actuators." The activation of SMA generates a contraction of the wires that in turn causes, because of the eccentricity with respect to the spring subsystem center of rotation, a relative angular movement of the bulk plates.

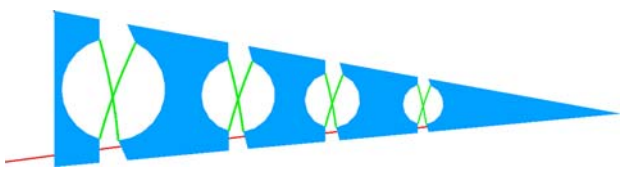

Fig. 1 Rib architecture

SMA ribbons and rods are also considered in the following discussion.

The used springs show a nonlinear behavior, because of the translation of the rotation pivot during deflection. This property goes into the direction of achieving in principle higher preloads for SMA wires recovery and larger relative rotations, while assuring the desired rigidity levels. These properties are strongly dependent on some geometric parameters, as shown in the next paragraph; then, by properly adjusting those values, the performance may be improved or optimized.

MSC/Nastran FE models were set up to investigate the behavior of the described structural system, integrated with an external proprietary Matlab routine aimed at simulating the behavior of the SMA elements, implementing the Liang and Rogers' 1D model (Ref 12). The assumptions, this model is based on, are coherent with the working modality of the actuators: no bending actions (the wires are hinged with the rib panels) and 1D behavior of the material (strain recovery is thought to occur only along the axial direction). Liang and Rogers' is an approximation of the former Tanaka's model (Ref 13), substituting exponential with sinusoidal expression in the description of the material composition (austenite versus martensite fraction, ξ_M and ξ_A), function of the temperature, T, and the stress field, σ:

$$\xi = \frac{\xi_M}{2}\cos[a_A(T - A_S) + b_A\sigma] + \frac{\xi_M}{2} \quad \text{Austenite} \rightarrow \text{Marteniste} \tag{Eq 1}$$

and

$$\xi = \frac{1 - \xi_A}{2}\cos[a_M(T - M_F) + b_M\sigma] + \frac{1 + \xi_A}{2}$$

$$\text{Marteniste} \rightarrow \text{Austenite}$$

The values $a_A = \pi/(A_F - A_S)$ and $a_M = \pi/(M_S - M_F)$ are combinations of the material characteristic constants, A_F, A_S, M_F, M_S, namely, austenite final, austenite start, martensite final, and martensite start temperature, respectively. They refer to the beginning or the completion of phase transformation and define when a particular crystal structure appears or when the conversion is complete. Two other parameters appearing in the above formulas are $b_A = -a_A/C_A$ and $b_M = -a_M/C_M$, C_A and C_M being the slopes of the linear relationship between stress and temperature characteristic transformation.

Non-linearity assumption is necessary in order to properly consider the large strains, the characteristic of an SMA application. SMA-active elements are simulated through thermal 1D elements characterized by a negative expansion coefficient (SMA contracts as the temperature increases). Following activation, the structure deforms under the action of the wires. They both undergo a stressed condition. The attained displacement is associated with the computed SMA material stress. This operation is repeated for increasing values of the activation temperature, so that the dot-line curve in Fig. 2 may be sketched. As the force increases, the strain also does and because of the large strains attained, the classical non-linear behavior is shown (smaller strains for an equal increase of the forces). The initial configuration is assumed to have an offset of a roughly 5% strain, while the starting point of the operative function is at 3%, corresponding to the imposed recoverable strain for repeated cyclic applications (Ref 14, 15). In reality, the SMA wires will exhibit growing contractions until it

transforms completely into austenite. This is represented by the intersection point of the dot-line curve with the dotted curve that is the graphical representation of the constitutive material law for a generic SMA. The intersection point determines then the working condition of the proposed actuator. This kind of procedure allows reaching the "maximum" recoverable strain. The process may instead be stopped at a certain point, not letting the material undergo the complete phase transformation (partial recovery).

The process herein described is a simplification of the followed strategy. In fact, in order than the process may be cyclic, the activation point shall be moved at a prestressed configuration and, particularly, fixed at the complete martensite state. This assures the capability of recovering the maximum value of strain (complete transformation martensite-austenite is thus accessible). As the activation takes place (austenite start), the working point moves toward higher stress values. The final point is established when the desired strain recovery percentage is attained that is a function of the cycles number to be faced (Ref 14, 15).

From a figurative point of view, increasing temperature makes the SMA material curve to move up in the 2D stress-strain material plane and the working point to shift towards left, over the lower boundary of the SMA material curve (austenite transformation). On cooling the wire, the process is reversed under the action of a recalling force that makes the SMA to transform again into the martensite phase. The working point in this case runs over the upper part of the SMA material curve (martensite transformation). Thus, in the loading phase, the transformation may be said to be temperature driven; and in the recovery phase, stress driven.

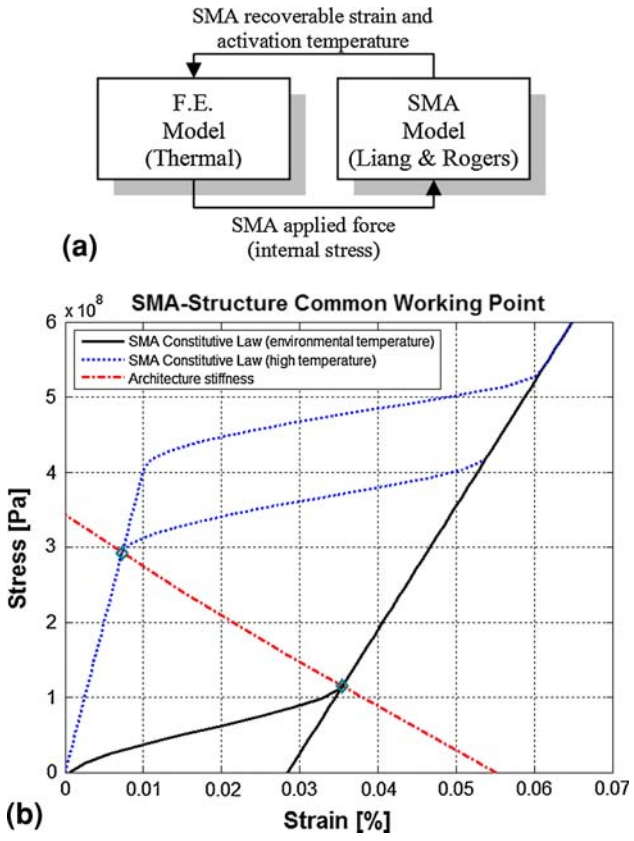

Fig. 2 Simulation scheme adopted for SMA integration within the FE approach

3. Aerodynamic Loads

The aerodynamic load computation has been addressed by assuming the RA 18-43NIL1 as wing airfoil; the RA 18-43NIL1 is a typical wing airfoil used in regional transport aircraft. In Fig. 3 the RA 18-43NIL1 geometry is plotted and some related parameters are indicated.

Points O and P are, respectively, called *leading* and *trailing edge* while the segment OP is referred to as the airfoil chord c. The chord divides the airfoil boundary curve in two parts: the *upper camber* (represented by the curve connecting O to P in a clockwise orientation) and the *lower camber* (represented by the curve connecting P to O in a clockwise orientation). The airfoil *mean camber line*, or more synthetically, the airfoil *camber line* is defined as the locus of the centers of circles tangent both to upper and to lower cambers.

Referring to the coordinate system of Fig. 3, the function $z_C = z_C(x)$ describing the camber line is given by $z_C(x) = [z_U(x) + z_L(x)]/2$, where $z_U = z_U(x)$ and $z_L = z_L(x)$ are the functions describing the upper and lower cambers. An airflow characterized by a velocity vector V induces a pressure distribution on the airfoil, along the upper and the lower camber, essentially related to: the shape of the airfoil, the magnitude of V, the air density, ρ, and the airfoil *angle of attack* defined as the angle between the airfoil chord and the direction of V.

Approximating the upper and the lower camber by means of n linear segments delimited by points A_i and A_{i+1} ($i = 1 \ldots n$ 1), the pressure p_i arising on each segment A_iA_{i+1}, can be expressed according to the following equation:

$$p_i = \frac{1}{2}\rho V^2 C_{p,i} = qC_{p,i} \qquad \text{(Eq 2)}$$

where $q = \rho V^2/2$ is called the *dynamic pressure* and $C_{p,i}$ the *local pressure coefficient*. The local pressure coefficient $C_{p,i}$ is a non-dimensional parameter whose value depends on the orientation of the segment A_iA_{i+1} in the airflow and therefore by the airfoil shape and angle of attack. The evaluation of the local pressure coefficients is usually performed by means of specific numerical methods of computational aerodynamics. In this study, they were evaluated by means of a two-dimensional vortex lattice method (VLM) (Ref 16).

A split-flap was considered, hinged at a distance of 0.7c from the airfoil leading edge; the wing airfoil portion between 0.7c and c was assumed to be representative of a flap airfoil and rotated around the hinge point in order to simulate the split-flap down deflection. Deflection angles δ between 2 and 24 deg

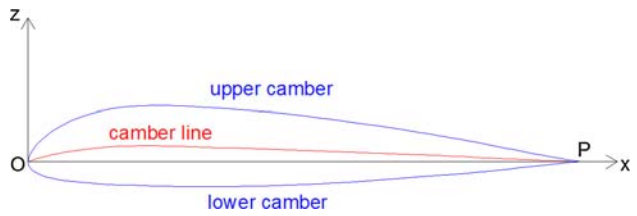

Fig. 3 RA 18-43NIL1 airfoil

were considered; for each step the C_p distribution and the wing airfoil lift coefficient, C_l, were evaluated in correspondence of a 5-deg angle of incidence (angle of attack). The airfoil lift coefficient C_l is defined by the following equation:

$$C_l = \sum_{i=1}^{n} C_{p,i}\left(\underline{n_i} \cdot \underline{\zeta}\right) \quad \text{(Eq 3)}$$

where n is the number of linear segments used to approximate the upper and the lower camber, $C_{p,i}$ is the pressure coefficient related to the i-th segment, n_i is the normal unit vector of the segment contained in the airfoil plane and positively oriented outwards of the airfoil surface, and ζ is the normal unit vector to the airflow velocity vector V. The airfoil lift coefficient, C_l, is a non-dimensional parameter used to characterize the lifting performance of airfoils or, in other terms, the airfoil's capability to generate a force orthogonal to the airflow velocity direction. Such a force, called *lift*, is responsible of aircraft sustentation and is proportional to C_l; higher C_l leads to higher lift. The obtained C_l values for each examined flap deflection are reported in Table 1 ($C_{l(conventional)}$).

Let us consider a two-dimensional Cartesian reference system S_0, defined as follows: origin located at the airfoil leading edge; X-axis directed along the non-flapped chord and oriented towards the trailing edge; Z-axis in the airfoil plane and oriented upward. In correspondence of a flap rotation δ_i, around the hinge point A $[0.7 \cdot c; Z_A]$, the trailing edge moves from the point P $[c; 0]$ to the point P', defined by the coordinates: $X_{P'} = 0.7 \cdot c + \overline{AP} \cdot \cos(\alpha + \delta_i)$, $Y_{P'} = \overline{AP} \cdot \sin(\alpha + \delta_i) - Z_A$ where $\alpha = \sin^{-1}\left(0.3 \cdot c/\overline{AP}\right)$. Fixed by the same trailing edge position due to a δ_i flap deflection, a quadratic morphing law was imposed to the camber line related to the flapped airfoil. In detail, the motion of point P to point P' was obtained by morphing the flapped airfoil camber line according to a parabolic arch connecting the point A to the point P', and the tangent in A to the wing airfoil camber line (Fig. 4). Camber line morphing was obviously obtained by means of a congruent morphing of the upper and lower cambers of the flapped airfoil.

According to this procedure, for each of the previously investigated hinged flap rotations, a corresponding morphed flap shape was found and the related global C_l was evaluated. The obtained results are reported in Table 1 ($C_{l(morphed)}$). In Fig. 5, the wing airfoil C_ls related to conventional split and morphed flap are compared for each δ_i. For a given trailing edge down-deflection, the morphed flap solution leads to higher wing airfoil C_l than the conventional split solution.

The morphed flap configuration leading to a wing airfoil $C_l = 2.09$ was considered the most satisfactory from an aerodynamic performance point of view, and was chosen as the target of this. It corresponds to a 12-deg deflection angle and a 160-mm vertical trailing edge displacement.

A morphed flap portion of span $b = 300$ mm was then considered for aerodynamic load evaluation purpose. Let us call, MS_a and MS_b, the two morphed flap airfoil shapes which delimit the flap portion. Considering the generic aerodynamic strip s_i, delimited by two homologues segments A_i,A_{i+1} and B_i,B_{i+1} lying, respectively, on MS_a and MS_b boundaries, according to (2), the aerodynamic load acting normally to s_i was evaluated as

$$F_{n,i} = qS_iC_{p,i} \quad \text{(Eq 4)}$$

where q is the dynamic pressure, S_i is the strip area, given by the product of the span, b, between the segments A_i,A_{i+1} and B_i,B_{i+1}, and length d_i; $C_{p,i}$ is the pressure coefficient, assumed equal for both segments A_i,A_{i+1} and B_i,B_{i+1}. A dynamic pressure of around 1500.00 N/mm^2 was considered, typical for take-off and landing of a regional transport aircraft. Using Eq 4, the aerodynamic load distribution acting on the flap portion was evaluated; this load distribution was then used for a proper sizing of the ribs to be located at the end of the investigated wing portion.

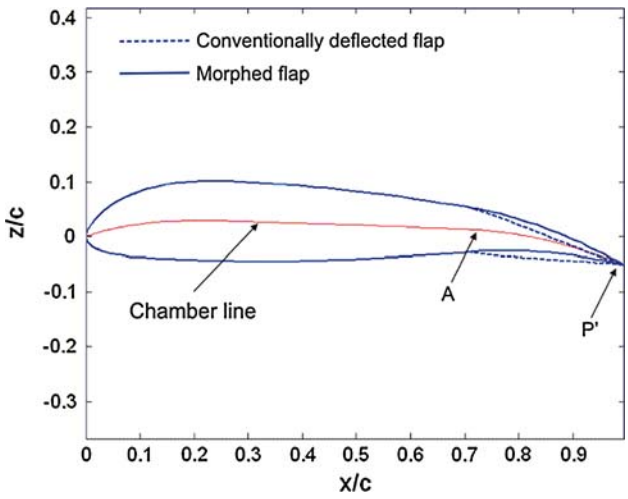

Fig. 4 Wing airfoil shapes corresponding to conventionally deflected flap and morphed flap

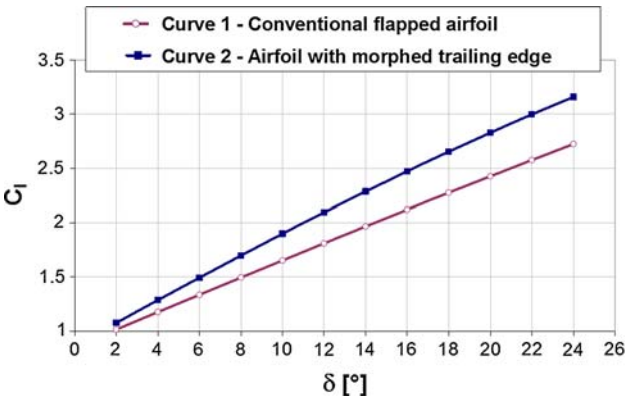

Fig. 5 Wing airfoil C_l comparison

Table 1 Wing airfoil C_l for several flap deflection angles

δ, °	2	4	6	8	10	12	14	16	18	20	22	24
C_l (conventional)	1.0155	1.1760	1.3359	1.4950	1.6532	1.8103	1.9663	2.1209	2.2740	2.4253	2.5749	2.7224
C_l (morphed)	1.0760	1.2866	1.4944	1.6990	1.8996	2.0956	2.2868	2.4727	2.6530	2.8275	2.9962	3.1589

4. Design Criteria of the Elastic Hinge

A parametric study was carried out on the aforementioned architecture. Since the elastic hinges play a fundamental role, the first efforts were focused on the identification of their optimal configuration. Through a FE approach, a single element was studied: its performance was estimated with respect to the cross plates length, d, and their relative angle, γ (Fig. 6). Discrete values for both parameters were assumed: 100, 120, and 140 mm for d; 60, 90, 120, and 150 deg for γ. A total of 12 runs were carried out to exploit all the possible combinations. Values higher than 150 deg were not considered, because of practical integration problems. The spring thin plates were assumed to be made of titanium, to meet both typical aeronautic lightness requirements and high allowable stresses, within the elastic range of the material.

The first phase was aimed at evaluating the performance dependence on the hinge geometry. Laminas, rectangular cross section was considered constant and set to 3×8 mm^2. Dimensions were defined according to design considerations based on the required flexibility and rigidity of the structure, together with the necessity of attaining a sufficient SMA preload and the capability of sustaining sufficient stress levels during actuation. SMA element features were fixed as follows: a wire 280-mm long, with a 0.5-mm diameter, called to recover a max strain of 3% (Ref 14, 15) with respect to its original length (martensite phase); further details can be found in Table 3.

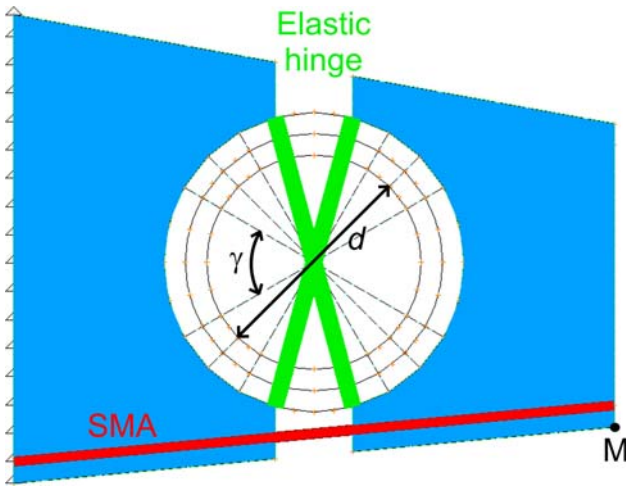

Fig. 6 Single elastic hinge scheme adopted for the parametric study

The results obtained are expressed in terms of hinge rotation and vertical displacement of the trailing edge. They are normalized and presented as histograms in Fig. 7, while actual values are reported in Table 2.

As a result of this first study, the max performance is achieved by maximising both d and γ: in this case, a displacement of 16.48 mm and a rotation of 5.91 deg is obtained (d = 140 mm; γ = 150 deg).

Assuming then the above parameters as the optimal configuration, further investigations were carried out by changing the SMA element characteristics and dimensioning the plate's cross section to withstand SMA preload and actuation requirements.

The active component properties were not made to change as a parametric variation but for modifying its nature, instead. Ribbon and rod forms were tested. The architecture of the actuators was maintained the same in each of the three cited cases, as well as the mechanism by which the load is transferred to the structure (two hinges). In Table 3, the features of the different SMA elements taken into account are reported, basing on experimental tests of material characterization carried out in our laboratory (Ref 17-19); length was set as the original, at 280 mm.

For the sake of clarity, it is useful to explain the exact meaning of the martensite and austenite Young moduli. The behavior of an SMA material is generally nonlinear, having to consider transformation between a phase and another and, contemporaneously having to take into account both the phases. However, when the transformation fully occurs (in a sense or the other), the material behaves as a classical linear one with distinct elastic moduli for the austenite and martensite status, respectively, E_A and E_M. Typically, E_M is one-third of E_A. Given the maximum recoverable strain ε_{max} for a given SMA, maximum recoverable force may be attained as:

$$F_{max} = E_A A \varepsilon_{max} \quad \text{(Eq 5)}$$

SMA commercial products were considered in the comparison. The use of different SMA materials for the different forms (wires, ribbons, rods) does not allow for an immediate comparison of the results but gives an idea of what can be expected in the different cases.

As already mentioned, preload is necessary to guarantee a full cyclic behavior inside the boundaries of the environmental and the austenite finish temperature (A_f), i.e., to guarantee the working point to run a complete loop over its martensite-austenite-martensite transformation. Because of this necessity, preload requires stiffer elastic elements for stiffer active elements: Table 3 shows the necessary preload for the diverse material typology and cross section. Furthermore, max stress

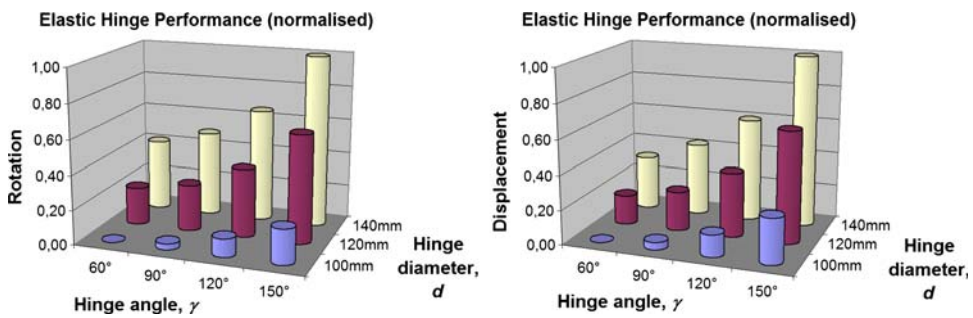

Fig. 7 Normalized performance of the elastic hinge vs. length, d, vs. relative angle

Table 2 Performance of the elastic hinge vs. length, *d*, vs. relative angle, γ

	Rotations				Displacements			
***d*/γ, mm**	**60°**	**90°**	**120°**	**150°**	**60°**	**90°**	**120°**	**150°**
100	5.7452	5.7509	5.7624	5.7778	0.01615	0.01617	0.01619	0.01624
120	5.7807	5.7887	5.8094	5.8466	0.01621	0.01623	0.01627	0.01636
140	5.8122	5.8248	5.8512	5.9068	0.01626	0.01629	0.01635	0.01648

Table 3 SMA actuators features (Ref 17-19)

	Wire	**Ribbon**	**Rod**
Cross section dimensions	0.5 mm diameter	1.0 × 10 mm	5.0 mm diameter
Cross section area	0.196 mm^2	10 mm^2	19.63 mm^2
Young's Modulus of Austenite E_A	24.67 GPa	40.18 GPa	28.16 GPa
Young's Modulus of Martensite E_M	18.27 GPa	16.5 GPa	8.78 GPa
Martensite start temperature	35 °C	43.3 °C	10 °C
Martensite finish temperature	12.6 °C	27.5 °C	−20 °C
Austenite start temperature	59.3 °C	47.3 °C	39 °C
Austenite finish temperature	85.9 °C	58.9 °C	82 °C
Stress necessary to achieve 3% strain (preload)	175 MPa	155 MPa	165 MPa
Force necessary to achieve preload	35 N	1550 N	3239 N
Maximum recoverable force (actuation)	∼550 N	∼8000 N	∼15000 N

Table 4 Results summary of the plate cross section dimensioning

	Wire	**Ribbon**	**Rod**
Elastic hinge cross section dimensions	3.0 × 8.0 mm	8.0 × 20 mm	8.5 × 32 mm
Elastic hinge cross section area	24 mm^2	160 mm^2	272 mm^2
Elastic hinge material	Titanium	Titanium	Titanium
Elastic hinge estimated weight	29.75 g	198.37 g	337.23 g
SMA preload			
SMA force level	35.65 N	1550.08 N	3238.69 N
Elastic hinge max stress	128 MPa	317 MPa	366 MPa
SMA actuation			
SMA force level	79.43 N	3426.84 N	6686.59 N
Elastic hinge max stress	289 MPa	715 MPa	769 MPa
Hinge performance			
Net displacement	13.217 mm	12.788 mm	12.495 mm
Net rotation	5.89 deg	5.67 deg	5.55 deg

following actuation shall be kept inside the titanium elastic range. The elastic hinges were then dimensioned according to a trial and error procedure: an arbitrary cross section was preliminarily assumed and stress conditions were evaluated at preload and activation phases. According to the preliminary outcomes, the cross sections were modified, taking into consideration the inertia moment and aiming at minimizing the total weight and bulk. The final results are summarized in Table 4, for the three configurations. The actuation performance in terms of hinge rotation and trailing edge displacement are finally shown in Fig. 8.

Elastic hinge resulting stress field presents the classical composed normal-bending shape, being caused by an eccentric normal force. Its maximum value is reported in the table and an example of the stress state into the plate components is shown in Fig. 9, where normal stress is shown.

From these results the wire architecture appears to lead to the best actuator performance. This trend is also confirmed when comparing the three configurations in terms of weight and SMA activation temperature (which in turn influences the required energy), estimated through the Liang & Rogers' model-based Matlab routine (Fig. 10).

Although the SMA represents a small amount of the overall weight, related preload and working constraints heavily condition the elastic hinge size. The SMA choice demonstrates once more to be a critical design aspect: an excessive powerful actuator may not lead to better performance while increasing total weight.

5. Design Criteria of the Rib Structure

The higher hinge performance, measured in terms of trailing edge vertical displacement and rotation is thus obtained for the highest values of d and γ in the considered interval and for a configuration wire-based SMA. By following these results, the design of the rib was accomplished.

In order to maximize the architecture features, it is necessary to accommodate the largest number of elastic hinges, each

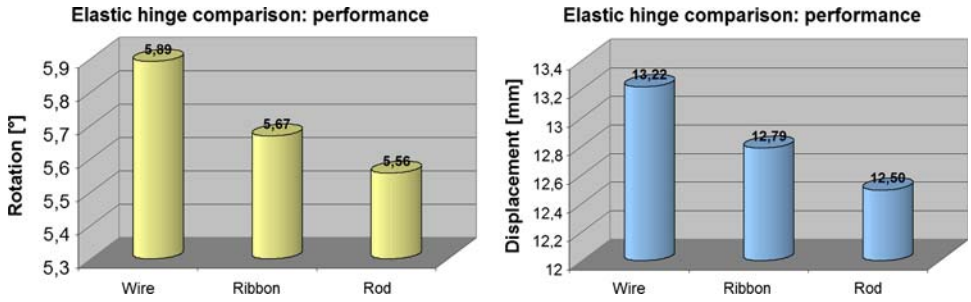

Fig. 8 Performance of the elastic hinge vs. SMA element typology

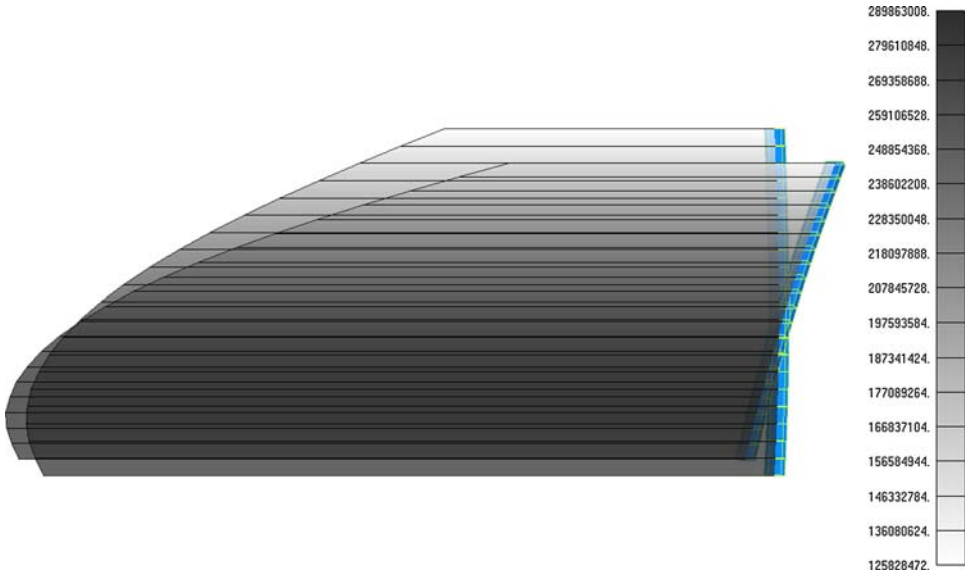

Fig. 9 Stress field distribution into the component plates of a reference hinge (wire solution)

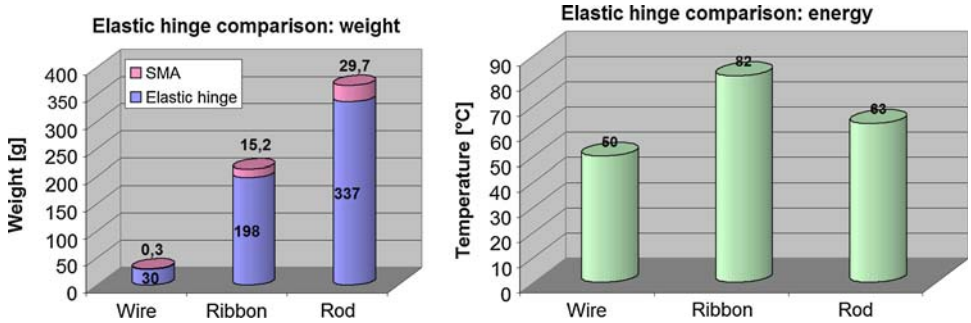

Fig. 10 Weight and SMA activation temperature comparison

characterized by the largest *d* parameter (of course, compatible with the local airfoil thickness) and the defined relative angle γ, in the considered section.

Finally, the actuator length also affects the attainable figures in a direct way (the longer the wire, the higher the performance). In Fig. 11, a sketch of the final rib arrangement is reported, while the design parameters are reported in Table 5.

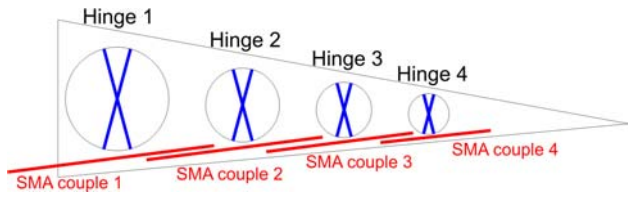

Fig. 11 Elastic hinges disposition within the rib

Table 5 Design parameters for each elastic hinge of the rib

	Hinge 1	Hinge 2	Hinge 3	Hinge 4
Elastic plates length, d	140 mm	100 mm	75 mm	55 mm
Elastic plates cross section	3.0 × 8.0 mm	3.0 × 6.0 mm	2.5 × 6.0 mm	2.0 × 7.0 mm
Elastic plates angle, γ	150 deg	150 deg	150 deg	150 deg
SMA wires length	280 mm	240 mm	200 mm	150 mm

Two SMA wires were considered for each elastic hinge, in order to properly counteract the aerodynamic loads, also being compatible with typical fail-safe design criteria, because of being associated with a certain redundancy level. SMA element splitting together with the geometrical variation of the d parameter, limited by the local airfoil thickness, led to a new sizing of the plate cross sections. Final results are reported in Table 5.

6. Numerical Simulation and Results

Once the final configuration was defined, a FE model was realized; analysis was carried out through MSC/Nastran. 7075 T6 aluminium alloy, 2-mm thick plates were considered for the rib panels. SMA wires were simulated through beam elements with a suitable thermal expansion coefficient (negative). This allowed for simulating the SMA contraction following the activation input; however, the nonlinear numerical analysis was performed by step, until reaching the equilibrium value, shown in Fig. 2(b). SMA beams were hinged at the rib panels in order to avoid any bending stress. In the same way, the titanium elastic hinges were simulated through beam elements.

In order to meet the necessity of attaining cyclic behavior and accessing the maximum recoverable strain, the configuration shall undergo prestress. In the real case, this can be attained by deforming the structure downward and then installing the SMA element. The elastic force tries to restore the initial configuration, deforming the SMA that, in turn, resists this recovery. Now, both the structural elements (elastic hinge) and the SMA wires go through a prestress condition.

The designer's ability is crucial to individualize the structural deformed configuration that is able to generate the stress in the SMA wire that assures equilibrium with the "residual" elastic force at the required "neutral" position (Fig. 12b).

In the numerical simulation, to replay the physical process is difficult enough. Instead the following alternative process may be followed. A non-deformed structure is realized according to the schematic shown in Fig. 12(a). Numerically, this configuration is not loaded (no internal stress) at the level of the crossed laminas or the SMA wires. Starting from this configuration, the rib is brought to the "neutral" condition (Fig. 12b), by activating the SMA via a fictitious negative thermal load. In this condition, both the structure and the wires experience a stress field. In spite of the different theoretical paths, followed to reach this condition, the numerical and the real configuration are conceptually the same. The numerical approach may be said to properly imitate the reality. Finally, a further activation of the SMA wires simulate the action of the active devices aimed at deflecting the proposed flap.

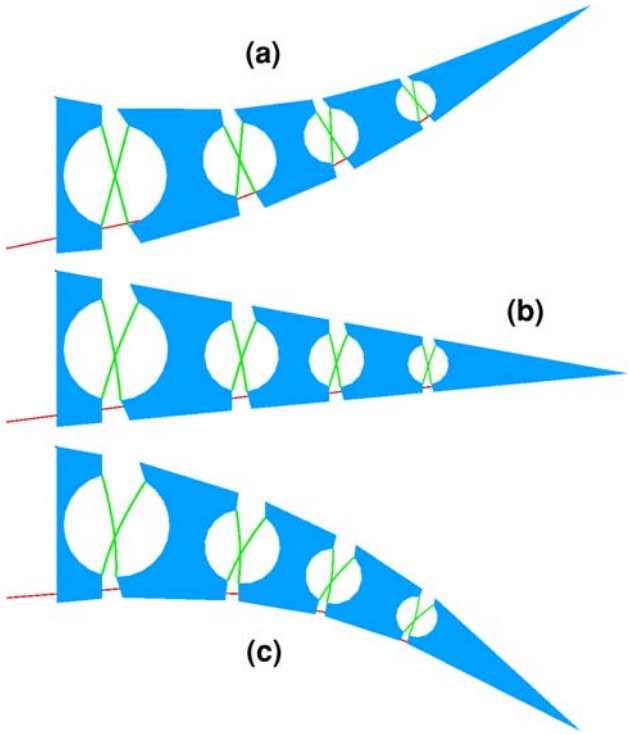

Fig. 12 Adaptive rib reference layouts: unloaded configuration (a); "neutral" position (b); activated rib (c)

Table 6 Preload condition details

	Hinge 1	Hinge 2	Hinge 3	Hinge 4
SMA force level[a]	82.6 N	81.94 N	81.65 N	79.91 N
Elastic hinge max stress	250 MPa	252 MPa	278 MPa	263 MPa
Hinge pre-load angle	10.17 deg	7.32 deg	7.42 deg	6.58 deg

[a]Each hinge has 2 SMA wires as actuator, doubling the necessary preload

Due to the modularity of the referred architecture, intermediate configurations are possible, between neutral and totally extended outline, according to the couples of SMA wires that are activated.

In Table 6, preload details are reported for both the laminas and SMA elements. It can be remarked that the maximum stress level reached in the elastic hinges under activation is always under 700 MPa.

Trailing edge vertical displacement and rotation, with and without aerodynamic loads, are reported in Table 7 for different activation conditions. Figure 13 shows finally the morphed

Table 7 Morphed flap performance: trailing edge displacement and rotation

	Performance without aerodynamic loads		Performance with aerodynamic loads	
	Vertical displacement, mm	Rotation, °	Vertical displacement, mm	Rotation, °
All SMA couples activated	246.7	32.24	223.9 (−9.24%)	29.84 (−7.44%)
Only first couple	84.83	7.01	71.24 (−16.20%)	5.71 (−18.54%)
Only second couple	72.31	7.95	61.2 (−15.30%)	6.83 (−14.08%)
Only third couple	58.33	8.51	49.53 (−15.08%)	7.62 (−10.45%)
Only forth	41.23	8.77	32.37 (−21.48%)	7.88 (−10.15%)

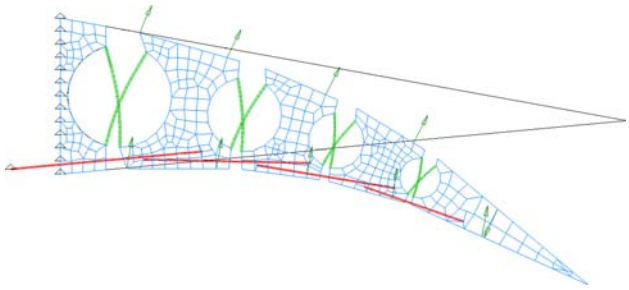

Fig. 13 Rib morphed shape for all SMA wires activated under aerodynamic loads

Table 8 Load conditions for the SMA wires during actuation

	Axial force[a] during actuation (without aerodynamic loads), N	Axial force[a] during actuation (with aerodynamic loads), N
SMA wires for hinge 1	153.27	651.73
SMA wires for hinge 2	183.28	446.09
SMA wires for hinge 3	186.65	310.01
SMA wires for hinge 4	199.21	238.77

[a]Force levels must be divided for the SMA actuators (2 wires for each hinge)

shape of the rib in presence of aerodynamic loads when all the SMA wires are activated.

The rib performance is well over the target of 160-mm trailing edge vertical displacement, estimated to lead to a lift coefficient of 2. Aerodynamic loads affect this result by 9.24% (a 7.44% difference is instead evaluated for rotation). This effect can be easily attributed to the flexibility introduced by the crossed laminas and the major stress level the SMA wires are subjected to (Table 8), however, compatible with their actuation capabilities.

When activating a single couple of SMA wires, vertical displacement and rotation show an opposite behavior; the more the ''active'' hinge is backward, the more the rotation increases while the vertical displacement reduces.

7. Conclusions and Further Steps

In this article, the design and the optimization of an SMA-based architecture, aimed at producing a morphing flap, have been presented.

The main innovation proposed by this study consists of the specific features of the rib architecture, following the principles of a ''smart structure'' (integrated, light, compact actuators), which is able both to largely deform itself (morphing) as well as to withstand external loads (bearing actuators).

A multi-body rib is referred to, whose components are linked to each other through elastic hinges made of crossed thin plates. In spite of the large forces produced, all the involved materials work inside the linear range. Geometrically, the configuration has intrinsic nonlinearities, caused by the pivots' translations. This effect has two main consequences: it decreases the effective carried load and increases the net rotation.

In order to maximize the adaptive flap performance in terms of max achievable rotations and vertical displacements, evaluated at the trailing edge, a parametric study was carried out, involving crossed laminas length and their relative angle. The best configuration was found to correspond at the higher values for thin plates length and angle, within the considered intervals.

Another study was then accomplished, by considering three different SMA element typologies: wires, ribbons, and rods. The optimal choice, when performance, compactness, and lightness are considered, was proved to be the wire-based one.

The problem of integrating the optimized elastic hinges within the rib was then faced. In order to obtain the max vertical displacement of the trailing edge, the largest number of these devices was integrated in the spar, considering the compatibility with the local airfoil thickness. Thus, four hinges suitably scaled and characterized by a 150-deg plate's relative angle were figuratively installed in the rib. Each of them presented peculiar characteristics, following the different geometric features, selected in order to guarantee the linear working of the involved materials.

Nonlinear numerical simulations were finally carried out, which can take into account a large number of expected displacements. A dedicated FE model of the rib architecture and the surrounding structure (i.e., skin elements and stiffeners) was realized. MSC/Nastran code was selected for simulations, integrated with an external Matlab routine for replicating the SMA elements behavior. A dedicated procedure was also set up in order to integrate the two programs. External aerodynamic loads were estimated by using a panel method on the morphing airfoil.

The structure behavior with and without aerodynamic loads, under the action of the designed device, was estimated and compared indicating the performance reduction following the presence of the external pressure field. Max displacement proved, however, to stand well above the target of 160 mm, corresponding to a C_L (lift coefficient) of 2.

The sophisticated numerical implementation of the morphing trailing edge herein presented would deserve a wider use. For example, to answer questions linked to the real use of these systems, such as the influence of the SMA actuator geometry

on the cooling time, max achievable actuation frequency etc. This would provide new and interesting details in evaluating the active devices performance in view of the integration on actual elements and will be the subject of future investigations.

In the same way, the active rib design and functionality could be further improved. Attention should be paid to the skin elements: sliding panels or more performing aerodynamic solutions like "elastomeric" skins, which can absorb cyclically large deformations could be examined.

Moreover, the possibility of expanding the proposed device working envelop, as its implementation like an aileron (able to undergo both positive and negative camber variations) shall be considered. Such architecture would require for instance SMA wires working in an antagonistic way, i.e., mounted, respectively, over and under the hinges' location. One of the most important additions to the complexity of the implemented model should be the one of pondering over whether to opt for the SMA Shape Memory or the Super Elastic Effect.

References

1. E. Stanewsky, Adaptive Wing and Flow Control Technology, *Prog. Aerospace Sci.*, 2001, **37**, p 583–667 (Elsevier Science Ltd.)
2. S. Kuzmina, G. Amiryants, J. Schweiger, J. Cooper, M. Amprikidis, and O. Sensberg, Review and Outlook on Active and Passive Aeroelastic Design Concept for Future Aircraft, *ICAS 2002 Congress*, September 8-13, Toronto, Canada, ICAS Vol. 432, 2002, p 1–10
3. J. Schweiger, A. Suleman, S. Kuzmina, and V. Chedrik, MDO Concepts for an European Research Project on Active Aeroelastic Structures, *9th AIAA/NASA/ISSMO Symposium on Multidisciplinary Analysis and Optimisation*, CP Atlanta, GA, 2002
4. J. Spillman, The Use of Variable Chamber to Reduce Drag, Weight and Costs of Transport Aircraft, *Aeronaut. J.*, 1992, **96**, p 1–8
5. H.P. Monner, T. Bein, H. Hanselka, and E. Breitbach, *Design Aspects of the Adaptive Wing—The Elastic Trailing Edge and the Local Spoiler Bump*, Royal Aeronautical Society, Multidisciplinary Design and Optimization, London, 1998
6. J.R. Wilson, Active Aeroelastic Wing: A New/Old Twist on Flight, *Aerospace Am.*, 2002, **40**(99), p 34–37
7. I. Chopra, Review of State of Art of Smart Structures and Integrated Systems, *42nd AIAA/ASME/ASCE/AHS/ASC Structures, Structural Dynamics, and Materials Conference*, Seattle, WA, *AIAA J.*, **40**(11), 2002
8. J. Browman, B. Sanders, and T. Weisshaar, Evaluating the Impact of Morphing Technologies on Aircraft Performance, *43rd AIAA/ASME/ASCE/AHS/ASC Structures, Structural Dynamics, and Materials Conference*, Denver, CO, USA, AIAA Paper 2002-1631, 22-25 April 2002
9. W.J. Buehler, J.V. Gilfrich, and R.C. Wiley, Effect of Low-temperature Phase Changes on the Mechanical Properties of Alloys Near Composition TiNi, *J. Appl. Phys.*, 1963, **34**, p 1475
10. S. Barbarino, S. Ameduri, and R. Pecora, Wing Chamber Control Architectures based on SMA: Numerical Investigation, *International Conference on Smart Materials and Nanotechnology in Engineering (SMN2007)*, 1-4 July 2007, Harbin, China, SPIE No. 6423-077
11. S. Barbarino, R. Pecora, L. Lecce, S. Ameduri, and A. Concilio, Airfoil Morphing Architecture Based on Shape Memory Alloys, *2008 ASME International Conference on Smart Materials, Adaptive Structures & Intelligent Systems (SMASIS08)*, October 28-30, Ellicot City, MD, USA, SMASIS08-480
12. C. Liang and C.A. Rogers, One-Dimensional Thermomechanical Constitutive Relations for Shape Memory Material, *J. Intel. Mater. Syst. Struct.*, 1990, **1**(2), p 207–234
13. K. Tanaka, A Thermomechanical Sketch of Shape Memory Effect: One-Dimensional Tensile Behaviour, *Res. Mechanica*, 1986, **18**(3), p 251–263
14. A.V. Srinivasan and D.M. McFarland, *Smart Structures: Analysis and Design*, Cambridge University Press, ISBN 0-521-65977-9, 1995
15. K. Shimizu and T. Tadaki, *Shape Memory Alloys*, H. Funakubo, Ed., Gordon and Breach Science Publishers, New York, ISSN 0889-860X, 1987, p 1–60
16. A.M. Kuethe and C.Y. Chow, *Foundations of Aerodynamics*, 4th ed., Wiley and Sons, 1986
17. S. Ameduri, P. Caramuta, and F. Lenzi, Experimental Characterisation of an SMA Rod Element for Helicopter Blade Morphing, *Internal Report*, CIRA-CF-08-0185, 2008
18. S. Ameduri, Test report di accettazione per nastri di SMA, *Internal Report* (in Italian), CIRA-TR-06-0215, 2006
19. A. Vigliotti and L. Lecce, Prove su campioni di SMA, *Internal Report* (in Italian), CIRA-TR-06-0346, 2006